

# MAELi - Masked Autoencoder for Large-Scale LiDAR Point Clouds

Georg Krispel<sup>1</sup> David Schinagl<sup>1,2</sup> Christian Fruhwirth-Reisinger<sup>1,2</sup> Horst Possegger<sup>1</sup> Horst Bischof<sup>1,2</sup>  
 {georg.krispel,david.schinagl,christian.reisinger,possegger,bischof}@icg.tugraz.at  
<sup>1</sup> Graz University of Technology <sup>2</sup> Christian Doppler Laboratory for Embedded Machine Learning

## Abstract

We show how the inherent, but often neglected, properties of large-scale LiDAR point clouds can be exploited for effective self-supervised representation learning. To this end, we design a highly data-efficient feature pre-training backbone that significantly reduces the amount of tedious 3D annotations to train state-of-the-art object detectors. In particular, we propose a Masked AutoEncoder (MAELi) that intuitively utilizes the sparsity of the LiDAR point clouds in both, the encoder and the decoder, during reconstruction. This results in more expressive and useful features, directly applicable to downstream perception tasks, such as 3D object detection for autonomous driving. In a novel reconstruction scheme, MAELi distinguishes between free and occluded space and leverages a new masking strategy which targets the LiDAR’s inherent spherical projection. To demonstrate the potential of MAELi, we pre-train one of the most widespread 3D backbones, in an end-to-end fashion and show the merit of our fully unsupervised pre-trained features on several 3D object detection architectures. Given only a tiny fraction of labeled frames to fine-tune such detectors, we achieve significant performance improvements. For example, with only  $\sim 800$  labeled frames, MAELi features improve a SECOND model by +10.09APH/LEVEL 2 on Waymo Vehicles.

## 1. Introduction

Thanks to recent large-scale and elaborately curated datasets, like the Waymo Open Dataset [41], we have seen tremendous progress in a variety of 3D perception tasks for autonomous driving. However, even with such cost-intensive datasets, models are only transferable to other domains with significant performance drops [48].

Self-supervised representation learning (SSRL) provides a technique to avoid the costly large-scale labeling effort. The overall idea is to learn universal feature representations in an unsupervised way, which are later utilized for a specific downstream task, such as object detection. For example, one of the most common approaches

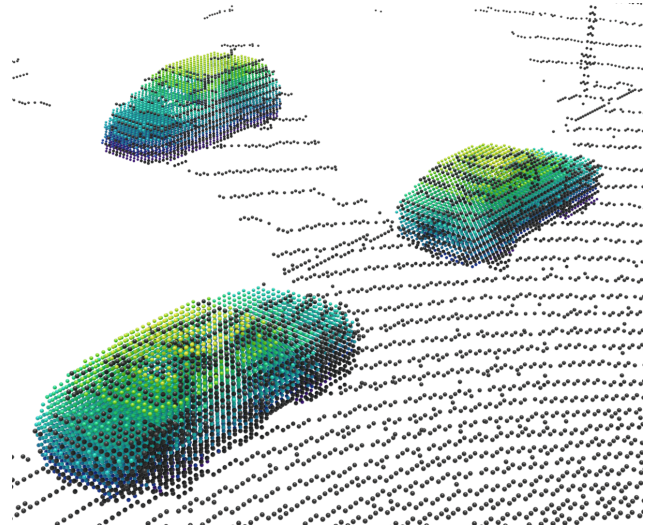


Figure 1. Reconstructed point cloud. In contrast to existing self-supervised representation learning (SSRL) approaches which simply reconstruct the initial point cloud (black), MAELi learns an expressive feature representation which captures the full geometric object structure of objects, without any ground truth labels. For visualization purposes, we color-coded the points by their  $z$ -coordinate and removed the reconstructed ground plane.

in 3D is to learn representations via *point cloud completion* [1, 25, 31, 46, 50, 66]. There, the task is to restore removed parts of a point cloud and thereby learning an implicit understanding of the scene and the object’s inner geometric structure. This is especially useful for full 3D point clouds generated from CAD models, such as ModelNet [51] or ShapeNet [3]. Recently, these methods were adapted for large-scale point clouds within the automotive domain [15, 30], already showing promising results.

Existing SSRL approaches, however, neglect several inherent, but fundamental properties of LiDAR point clouds. Contrary to previous methods, we leverage these properties and propose *MAELi*, a transformer-less masked autoencoder (MAE). Our memory-efficient, sparse decoder structure enables efficient pre-training of state-of-the-art object detectors in an end-to-end fashion on a single GPU. Further-

more, we do not just follow the straightforward approach of reconstructing the occupied space. Instead, we present a novel reconstruction scheme that allows us to go beyond the (visible) LiDAR points. As a result, MAELi learns how objects look like from any viewing direction, implicitly and in a genuinely unsupervised way, as illustrated in Figure 1.

Intuitively, we explicitly distinguish *occupied*, *free* and *unknown* space. While free space must be traversable and occupied space must reflect the respective LiDAR beams, we cannot make any assumptions about unknown space. Therefore, we do not induce any self-supervision in these regions during completion. In other words, our model does not penalize the reconstruction of structures which are either occluded or insufficiently sampled due to the limited LiDAR resolution.

During training, the model sees a large amount of objects, both in different poses and differently sampled. Despite the missing labels, our completion objective allows the model to reconstruct the whole objects, *i.e.* the entire geometric structure. In the process, MAELi learns features which better coincide with the underlying geometric structure instead of simply learning how to precisely reconstruct a masked point cloud surface (and thus, not learning the geometric contextual information).

For evaluation, we select the most critical automotive perception task, *i.e.* object detection. In extensive experiments on the Waymo Open Dataset [41], we demonstrate that MAELi features are well suited to effectively pre-train several state-of-the-art 3D detectors while requiring only a tiny fraction of labeled data. In summary, our contributions are threefold:

- We introduce a LiDAR-aware SSRL scheme to pre-train the encoder of a variety of state-of-the-art 3D object detectors.
- We introduce a novel reconstruction loss and masking strategy for unsupervised representation learning, especially designed for LiDAR properties.
- We show the effectivity of our decoder to pre-train expressive features for several baselines, improving them significantly when labeled data is scarce.

## 2. Related Work

**LiDAR-based 3D Object Detection:** Due to the rise of autonomous driving, formidable effort has been made researching and improving 3D object detection based on LiDAR point clouds. These methods can be divided on how the irregular structure of a point cloud is handled. *Point-based methods* [37, 39, 60, 67], initially inspired by the pioneering work of Qi *et al.* [32, 33], directly process points by means of their coordinates and input features, *e.g.* LiDAR

reflectivity. Based on this, Shi *et al.* [37] introduce a two-stage detector including proposal generation and box refinement. Point-GNN [39] defines a graph, thereby grouping neighboring points within a fixed radius, before feeding it to a dedicated graph neural network.

*Grid-based methods* [21, 49, 57, 58, 65, 70] define a regular grid, which enables common operations, *e.g.* convolutions, already successfully applied to 2D imagery. Several approaches [49, 58] project the data on the XY-plane respectively create a birds-eye-view, whereas VoxelNet [70] employs 3D convolutions. However, the computational effort grows cubically in 3D, but LiDAR point clouds only cover a small fraction of the relevant space. Thus, SECOND [57] utilizes sparse operations to significantly speed up inference time and memory consumption. Reusing the encoder from SECOND, Centerpoint [65] adapts the idea from [69] and reformulates the problem of 3D detection as the extraction of keypoints, *i.e.* the bounding box centers.

By contrast, [2, 7, 22, 28] solely utilize a point cloud’s *range view*, as it is a compact and lossless representation enabling an efficient feature extraction akin to the one in 2D imagery. However, depending on its distance, a single object varies in scale within the range view, but a model should always produce the same-sized 3D bounding box. This discrepancy requires several adjustments [7].

*Hybrid methods* [12, 17, 23, 29, 35, 36, 38, 61, 62] combine aspects of both, point- and grid-based approaches. For example, PV-RCNN [35, 36] incorporates features, which are derived from the respective layers of the voxel encoder and directly from the point cloud itself. Part- $A^2$  [38] classifies each point’s relative position within a bounding box as an auxiliary task. Hu *et al.* [17] utilize the estimated point-density in order to redefine their voxel’s centroid position and improve the subsequent RoI Grid Pooling [35] as well as the bounding boxes’ confidence prediction. Nevertheless, all these methods share the same encoder initially introduced with SECOND [57].

More recently, *Transformers* [45] were adapted to LiDAR-based 3D object detection [11, 26, 27, 34, 42]. Whilst achieving great results, vanilla Transformers usually have a large memory footprint and require a lot of processing power. In order to process large LiDAR point clouds, various tweaks mitigate the quadratically growing complexity depending on the number of input points. Sun *et al.* [42] even achieve real-time performance during inference with an highly optimized version of their SWFormer. Nevertheless, they still require either a dataset of substantial size or a proper pre-training strategy.

**SSRL for 2D Imagery and Points Clouds:** Self-supervised representation learning strives to learn useful features before introducing any supervision in the form of manually labeled ground truth data. These features are utilized to improve the results on respective downstream tasks

or reduce the amount of required training data.

*Contrastive learning* approaches task a model to maintain similar embeddings for the same data instance when transformed with different augmentations. Consequently, different data instances should lead to diverging embeddings. Initially applied to 2D imagery [4, 14, 16, 47], these methods were also adapted for point clouds [19, 24, 53, 64, 68]. Naturally, the granularity of the induced consistency loss defines the *semantic level* on which the model agrees upon. In other words, contrastive learning on a global embedding describing an entire image or point cloud is more suitable for downstream tasks like classification. Tasks like object detection or semantic segmentation, however, necessitate a more fine-grained treatment. The causality dilemma is to sample semantically coherent regions with a proper level of detail without knowing what is semantically coherent. For example, Yin *et al.* [64] generate proposals via farthest point sampling and ball queries after removing the ground plane.

**SSRL via Reconstruction:** Recently, generative self-supervised representation learning approaches are on the rise, outperforming their contrastive counterparts. One of the most successful concepts is the one of *denoising autoencoders*. Based on the encoder’s output embedding, the decoder is tasked to reconstruct the denoised input and if successful, the encoder is forced to learn a useful representation resilient to noise. Especially the completion of a masked input gained huge traction across various fields of application, among others like natural language processing (NLP) [6] and 2D imagery [13] also on point clouds. The major research focus, however, is to learn representations on synthetic datasets [9, 25, 31, 46, 56, 59, 66] like, *e.g.* ShapeNet [3] or ModelNet [51], just very recently a few works consider LiDAR point clouds [15, 30, 52].

Xie *et al.* [52] require full supervision, whereas we do not need any labels for pre-training. In [30] they only pre-train the sparse 3D voxel backbone ignoring the dense birds-eye view (BEV) part of a common 3D encoder. They instead apply a computationally demanding dense decoder. We utilize a memory efficient sparse decoder, which enables us to pre-train the entire encoder.

Only very few works consider a LiDAR point cloud’s inherent properties, *i.e.* its sampling resolution and 2.5D perception (due to occlusion). Wang *et al.* [46] synthesized occlusion on small-scale full 3D point scans and learn to complete them, thereby pre-training useful features for several downstream tasks. Hu *et al.* [18] compute visibility maps via raycasting in order to avoid inconsistent object augmentation [57] and to be added as additional input to a detection network. Xu *et al.* [54] complete points of ground truth objects by grouping similar ones and use them to learn an auxiliary task, which estimates the probability of an occluded area to be occupied by an object.

There are approaches which use point completion as a pre-processing step rather than learning a representation [44, 55]. In [44] they complete a LiDAR point clouds to transform it into a canonical form for a 3D object detector. However, they require synthetic or ground truth labels for training and, during inference, an elaborate network on top of the detector.

### 3. MAE for Large-scale LiDAR Point Clouds

We aim to significantly reduce the expensive labeling effort for large-scale LiDAR point clouds via self-supervised representation learning (SSRL). We build upon the successful masking and reconstruction approach but observed that existing approaches only learn to reconstruct the original input point cloud, nothing more. While this is well suited for full 3D models, such as those generated by CAD renderings [3, 51], this approach limits the usefulness of the learned features for LiDAR point clouds in two key aspects. First, due to the limited angular resolution of a LiDAR sensor, there are gaps between the LiDAR beams. Simply reconstructing the original point cloud would mean to penalize the model for (correctly) reconstructed points in these gaps. Second, a LiDAR sensor can not capture objects fully. Once a surface reflects a beam, there is no information about what is behind the surface. Thus, models based on standard reconstruction are hindered from learning implicit contextual information. With our MAELi, we observed that this implicit information results in more expressive features.

To allow simple integration into a wide variety of state-of-the-art models, we demonstrate MAELi to pre-train one of the most widely used point cloud encoders today, initially introduced by SECOND [57]. In the following, we briefly summarize the overall encoder structure (Sec. 3.1) before we explain our sparse decoder (Sec. 3.2), the reconstruction objective (Sec. 3.3) and our masking strategy (Sec. 3.4).

**Definitions & Notations:** Let  $\mathcal{V}^{E,s} = \{\mathbf{v}_j^{E,s}\}_{j=1\dots M^{E,s}}$  be the  $M^{E,s}$  active voxel positions of a certain *tensor stride*  $s$  in the sparse encoder and  $\mathcal{V}^{D,s} = \{\mathbf{v}_j^{D,s}\}_{j=1\dots M^{D,s}}$  the  $M^{D,s}$  active voxel positions in the sparse decoder, where  $\mathbf{v}_j \in \mathbb{R}^3$ . A voxel position is considered *active* if any of its related features deviates from zero and is thus taken into account by the sparse operations. Only the active sites are actually stored in memory.

We follow the notation of [5] for sparse convolutions, where the *voxel/tensor stride*  $s$  refers to the distance between two voxels w.r.t. the highest voxel resolution along each axis. For example, applying two (or three) 3D convolutions with a stride of 2 leads to a feature map with a tensor stride of 4 (or 8). Consequently,  $\mathcal{V}^{E,1}$  and  $\mathcal{V}^{D,1}$  denote the voxels in the encoder’s input layer and the final output layer of the decoder, respectively. A downsampling step increases the stride, while an upsampling step decreases it.

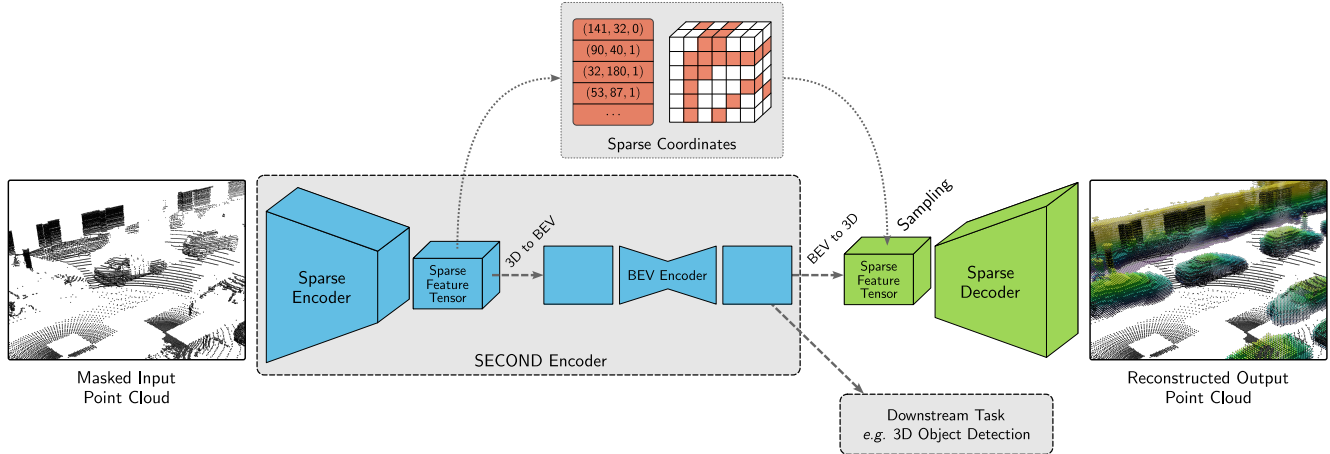


Figure 2. Overview of our MAELi pre-training. The task of our sparse decoder (green) is to reconstruct the missing parts of the masked input point cloud. Thereby, the encoder (blue) is forced to learn a reasonable representation usable for a down-stream task, *e.g.* 3D object detection. Since we do not penalize our network for reconstructing voxels at areas not visible to the LiDAR, it learns to reconstruct occluded parts without any ground truth labels, leading to more expressive features. We color coded the  $z$ -coordinate and removed the ground plane in the output for visualization purposes.

### 3.1. Sparse 3D and BEV Encoder

We use our MAELi to pre-train the features learned by the widely used SECOND [57] encoder, as illustrated in Figure 2. This encoder first voxelizes the point cloud and efficiently processes the highly sparse data via dedicated sparse convolutions (SC). Contrary to its standard dense pendant, a SC is only applied if the kernel covers any active site. Nevertheless, even with small  $3 \times 3$  kernels, these active sites dilute rapidly, increasing computational effort on the way. Thus, SECOND additionally includes submanifold sparse convolutions (SSC) [10], where the kernel center is only placed on the active sites. It only considers active sites covered by the kernel and maintains their amount and memory consumption.

After multiple downsampling steps, the spatially reduced voxel space and its features are transformed to a dense tensor, projected to a BEV representation and processed by a common small 2D encoder/decoder structure to increase the receptive field. The resulting features then act as inputs to the detection heads of various state-of-the-art models.

### 3.2. Sparse Reconstruction Decoder

Our goal is to obtain more expressive features via pre-training the entire SECOND encoder, *i.e.* both the sparse 3D voxel backbone and the 2D BEV backbone, in an end-to-end fashion. Thus, we attach a reconstruction decoder as illustrated in Figure 2 (detailed architecture is given in the supplemental material). Contrary to existing sparse encoder/decoder structures for LiDAR point clouds, *e.g.* Part-A<sup>2</sup> [38], we have to address two key differences.

First, we want to pre-train the entire encoder in order to utilize as much representation capabilities as possible.

Therefore, we need to adapt to the dense feature map provided by the BEV backbone. However, dense upsampling to the original spatial resolution is not feasible, as it would be too demanding in terms of both memory and computational effort. Instead, we transform the dense feature map into a sparse tensor, guided by the active sites of the sparse encoder: we reshape the dense tensor such that its dimensions coincides with the 3D output volume of the sparse encoder and sample certain coordinates, *i.e.* we subsequently set them active. In particular, we use the same coordinates which were active at the output of the sparse encoder and extract the respective features from the dense BEV output.

Second, to perform completion on a point cloud, we require a decoder which is able to also reconstruct the removed voxels. However, a common upsampling step by a factor of 2 applied to an active voxel would already generate 8 more fine-grained voxels with half size. To avoid memory issues due to the cubically increasing number of active voxels, existing approaches, such as [38], limit the upsampling layer such that only voxels are generated which were already active in the corresponding layer of the encoder. Consequently,  $\mathcal{V}^{E,s}$  would be equal to  $\mathcal{V}^{D,s}$  for all strides  $s$ . However, this strategy does not allow the decoder to reconstruct voxels which were not present in the encoder, rendering it unusable for a completion task.

For the decoder to reconstruct and complete, each upsampling layer grows (cubically), but a subsequent pruning layer learns to remove redundant voxels, as illustrated in Figure 3. For this, we closely follow the technique of small-scale point cloud reconstruction [5], which is to apply a  $1 \times 1$  convolution to the sparse feature map and learn the pruning. To obtain stronger feature representations, we propose an extended reconstruction objective which induces

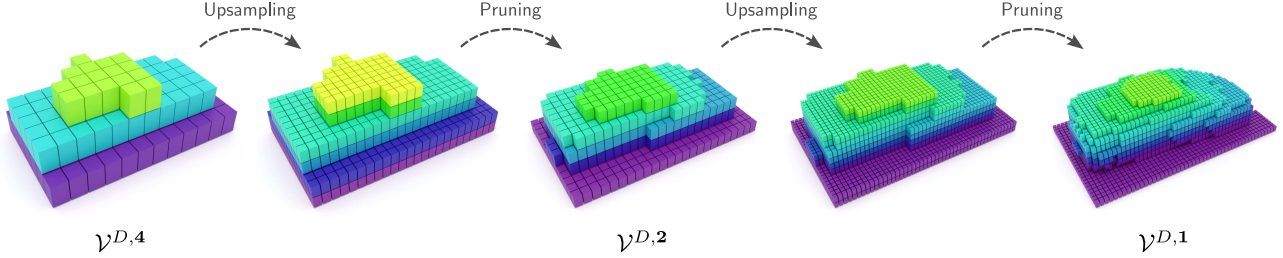


Figure 3. Reconstruction of a car within our decoder. An upsampling step halves the *voxel stride* and voxel size and increases the number of voxels. Subsequently, superfluous voxels are removed during the pruning step. We cropped the car and color coded the *z*-coordinate for visualization purposes.

more knowledge about the underlying structure of the perceived environment.

### 3.3. Reconstruction Objective

We design the reconstruction objective to allow the model to learn the geometric structure of objects. Intuitively, it should be easier for a model to learn what an entire car looks like instead of reconstructing the specific points scanned by the LiDAR. Therefore, we distinguish three categories of reconstructed voxels: *occupied*, *free* and *unknown*. They are illustrated in Figure 4.

Occupied voxels contain surface points from the original point cloud (before masking) and should thus be part of the reconstruction. Free voxels are the ones traversed by the LiDAR beam without hitting any surface and thus, should remain empty. Finally, we categorize a voxel as *unknown* if neither of the first two cases applies, *i.e.* these are either occluded or were not hit by the beam due to the limited angular resolution.

Additionally, we observe that the discrete voxelization can cause inaccuracies, especially at low resolution voxel grids. We mitigate this by decreasing the loss of a free voxel with the normal distance  $d_j^{d,s}$  between its voxel center  $\mathbf{v}_j^{D,s}$  and the nearest LiDAR beam. More formally, we define the weight  $w_j^{D,s}$  for a voxel as

$$w_j^{D,s} = \begin{cases} 0 & \text{if } \mathbf{v}_j^{D,s} \text{ is } \textit{unknown}, \\ 1 & \text{if } \mathbf{v}_j^{D,s} \text{ is } \textit{occupied}, \\ 1 - \frac{2 d_j^{D,s}}{d_v^s} & \text{if } \mathbf{v}_j^{D,s} \text{ is } \textit{free}, \end{cases} \quad (1)$$

where  $d_v^s$  denotes the length of a voxel diagonal at stride  $s$ .

We require the same categorization for voxels of lower resolution and larger strides, respectively. For example, a voxel of stride  $s$  spatially covers eight voxels of stride  $s/2$  after upsampling (see Figure 3). Here, however, we need to consider that if a low-resolution voxel is pruned, it can no longer generate a self-supervised signal for its higher-resolution voxels during upsampling. Thus, a low-resolution voxel is considered *occupied* if it incorporates

any high-resolution *occupied* voxel (red rectangle in Figure 4). Similarly, it is *unknown* (violet rectangle) if it incorporates any *unknown* voxel but no *occupied* ones. Otherwise, the low-resolution voxel is categorized as *free*.

In summary, the objective during self-supervised pre-training is to correctly classify whether a voxel is *occupied* or *free*, while simply ignoring the *unknown* ones. For this,

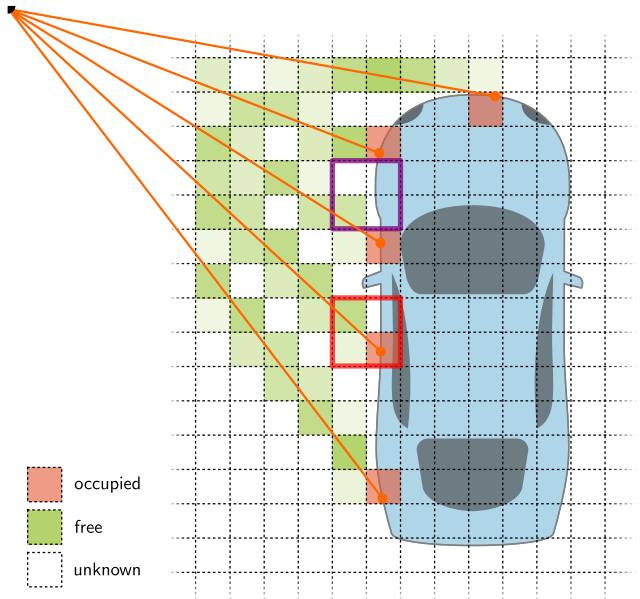


Figure 4. Schematic loss illustration: a loss should only be induced for voxels, where we *actually know* whether the space is free or not. LiDAR beams traverse *free* voxels (green) until they hit a surface, *i.e.* an *occupied* voxel (red). Other voxels are considered *unknown*. The loss for a *free* voxel is weighted by the proximity of its center to the nearest beam (different shades of green) to counter inaccuracies due to discrete voxelization. A voxel of lower resolution (here twice the stride) is considered *occupied* (red rectangle) if it incorporates at least one smaller voxel, which is *occupied* as well (red) and *unknown* if it incorporates an *unknown* voxel (violet rectangle).

we use a weighted binary cross-entropy loss

$$\mathcal{L} = -\frac{1}{\widetilde{M}^D} \sum_{s \in \mathcal{S}^D} \sum_{j=1}^{M^{D,s}} w_j^{D,s} l_j^{D,s}, \quad (2)$$

with

$$l_j^{D,s} = \left[ y_j^{D,s} \log x_j^{D,s} + (1 - y_j^{D,s}) \log(1 - x_j^{D,s}) \right], \quad (3)$$

where  $\mathcal{S}^D$  denotes the set of all strides and  $\widetilde{M}^D$  the total amount of all *occupied* and *free* voxel in the decoder;  $y_j^{D,s}$  is the actual occupancy of the voxelized input point cloud, *i.e.* 1 if  $\mathbf{v}_j^{d,s}$  is *occupied* and 0 otherwise; and  $x_j^{D,s}$  is our model’s predicted occupation probability. In other words, we penalize each pruning step for removing *occupied* and maintaining *free* voxels, but we do not induce any loss for *unknown* voxel.

### 3.4. Masking Strategy

In methods applied to small-scale full 3D point clouds, a common masking strategy is to apply Farthest Point Sampling (FPS) and the K-Nearest Neighborhood (KNN) algorithm to create (overlapping) patches [31, 66], which are then randomly removed. Applying FPS to LiDAR point clouds would, however, predominantly pick isolated points, which are usually single outliers far off. Masking these would not be beneficial to learn a strong feature representation, as such outliers usually do not correspond to real scene structures and have only few neighboring points. Instead, we exploit the voxel mechanisms already in place and mask the voxels randomly.

Furthermore, consider the sampling resolution of a standard spinning LiDAR sensor: It sends out multiple beams, waits for their return and then derives the distance to a hit obstacle, *i.e.* the *range*, from the elapsed time. Every beam has an inclination and rotates around a common vertical axis, defining an azimuth. Since two specific beams enclose a constant angle, the spatial resolution and thus, the number of points decreases with the distance to the hit object. Considering SSRL via point cloud completion, there is less self-supervision with increasing distance to the sensor.

Intuitively, if we remove points from nearby regions, such that they look similar to sparser regions further away, the model should be able to better generalize to these. We incorporate this *spherical masking* idea by reducing the angular resolution in both, azimuth and inclination. To do this efficiently, we subsample the LiDAR’s range image. In particular, we randomly sample two integers  $1 \leq m_r, m_c \leq 4$  and filter all rows  $r$  and columns  $c$  of the range image for which  $r \bmod m_r \neq 0$  or  $c \bmod m_c \neq 0$ , respectively. For example, using only every second row and column halves the angular resolution. This way, an object is sampled as if it would have been further away, but we are

able to induce more self-supervision during our reconstruction task.

## 4. Experiments

We show the merits of our pre-training on the 3D object detection benchmark of the Waymo Open Dataset [41], one of the most widely used and challenging datasets for autonomous driving. It contains 798 training sequences (158,361 frames) and 202 validation sequences (40,077 frames) and thus, is about 20 times larger than KITTI [8]. Each frame contains a LiDAR point cloud accumulated from the responses of five separate LiDARs, enabling a 360° view around the ego vehicle. It provides labels for three classes, *i.e.* *Vehicles*, *Pedestrians* and *Cyclists*. We follow the official Waymo evaluation protocol and report the results in terms of average precision (AP) and its pendant APH, which is weighted by the heading accuracy, both in the two difficulty levels, LEVEL 1 and LEVEL 2.

**Implementation Details:** We integrate MAELi into the OpenPCDet [43] framework (v0.5.2) and employ the Minkowski Engine [5] to design our sparse decoder. We pre-train the encoder for 30 epochs without any labeled ground truth. We utilize the Adam optimizer [20] and a one-cycle policy [40] with a maximum learning rate of 0.003. To fine-tune the different detectors with our pre-trained features, we warmup the detection head by freezing the encoder for 10 epochs and train end-to-end for 30 epochs. We ran our pre-training and subsequent experiments on an NVIDIA® GeForce® RTX 3090 GPU.

OpenPCDet provides several augmentation techniques for Waymo, *i.e.* random flip/rotation/scaling and *ground truth sampling* [57]. During pre-training, we utilize random flip/rotation/scaling in addition to our masking strategy (see Section 3.4). For fine-tuning, we adopt all of them, but we adjust *ground truth sampling* for a fair data efficiency evaluation as follows.

### 4.1. Data efficiency

Our ultimate goal is to significantly reduce the amount of labeled data needed to train state-of-the-art detectors. To this end, we demonstrate the benefits of using MAELi-pre-trained features for detectors in a low data regime. We split the training set into two groups: The first 399 sequences are used without any ground truth labels to pre-train our features. We then uniformly sample varying fractions of all remaining frames to fine-tune three different detectors, *i.e.* SECOND [57], CenterPoint [65] and PV-RCNN [35].

For a fair evaluation, we cannot apply the vanilla form of ground truth sampling from OpenPCDet, as it samples ground truth objects across the entire dataset and copy-pastes these randomly into frames which contain only few objects. Without change, this would add ground truth objects from other than our subsampled frames and thus, in-

Fraction Labeled Data	Method	3D AP/APH (LEVEL 2)				
		Gain	Overall	Vehicle	Pedestrian	Cyclist
1% (791 frames)	Centerpoint	- / - <b>+9.29 / +8.75</b>	39.64 / 36.50 48.93 / 45.25	41.01 / 40.32 49.99 / 49.24	40.01 / 32.63 51.92 / 43.07	37.90 / 36.55 44.89 / 43.43
	PV-RCNN	- / - <b>+7.53 / +4.89</b>	43.93 / 30.72 51.46 / 35.61	51.34 / 48.70 56.24 / 55.38	41.59 / 20.35 49.41 / 25.32	38.86 / 23.11 48.73 / 26.14
5% (3952 frames)	Centerpoint	- / - <b>+4.49 / +4.21</b>	53.91 / 51.16 58.40 / 55.37	53.04 / 52.45 57.62 / 57.01	52.73 / 46.51 59.01 / 51.83	55.96 / 54.53 58.57 / 57.27
	PV-RCNN	- / - <b>+1.64 / +1.39</b>	56.98 / 38.98 58.62 / 40.37	61.66 / 60.86 62.77 / 62.04	53.28 / 27.15 57.07 / 29.05	56.00 / 28.92 56.02 / 30.02
10% (7904 frames)	Centerpoint	- / - <b>+3.26 / +3.07</b>	58.09 / 55.41 61.35 / 58.48	56.95 / 56.40 59.93 / 59.36	56.97 / 50.90 62.06 / 55.30	60.35 / 58.94 62.06 / 60.78
	PV-RCNN	- / - <b>+1.19 / -0.05</b>	60.09 / 41.89 61.28 / 41.84	63.73 / 63.05 64.63 / 63.99	57.32 / 30.09 59.82 / 30.90	59.23 / 32.53 59.40 / 30.62
20% (15808 frames)	Centerpoint	- / - <b>+0.98 / +0.90</b>	61.81 / 59.15 62.79 / 60.05	60.59 / 60.06 61.79 / 61.23	61.19 / 55.03 63.47 / 57.04	63.64 / 62.36 63.11 / 61.87
	PV-RCNN	- / - <b>+0.49 / +7.21</b>	62.15 / 42.99 62.65 / 50.20	65.01 / 64.35 65.45 / 64.85	60.40 / 30.30 61.54 / 35.52	61.05 / 34.32 60.95 / 50.24

Table 1. Quantitative results of our features on Centerpoint [65] and PV-RCNN [35] on the Waymo *val* set. For each detector, we report the results of training from scratch (upper row) and the improved results utilizing MAELi-pre-trained features (lower row), respectively. We use the first 399 sequences of the Waymo *train* set for pre-training and different fractions of the second 399 sequences for fine-tuning.

validate the data efficiency study. Thus, we filter the original ground truth database and ensure that it only contains objects from the actually used frames.

We show the benefits of MAELi-pre-trained features in a low-data regime for CenterPoint [65] and PV-RCNN [35] in Table 1, by using different fractions of labeled data from the latter 399 sequences to fine-tune the detection heads. Table 2 summarizes the results for SECOND [57], where we can compare with ProficientTeachers [63], a state-of-the-art, but semi-supervised, approach for data-efficient 3D object detection.

We see that all baselines clearly struggle if only few labels are available, especially when considering the accuracy of the estimated heading. Naturally, this is most notable for underrepresented classes, *i.e.* *Pedestrians* and *Cyclists*. This is even more obvious if we consider the ambiguous heading of an average Pedestrian’s bounding box with a nearly square footprint. However, during the reconstruction task, our features need to carefully adapt to an object’s pose, or otherwise, the reconstruction would fail. Consequently, the 3D object detectors, in particular the anchor-based SECOND and PV-RCNN, pre-trained with MAELi benefit in terms of APH. For example, PV-RCNN+MAELi gains 7.21mAPH on 20% of the data compared to its vanilla pendant.

## 4.2. Improving 3D Object Detection

We also show the benefits of our expressive MAELi features by following the common protocol of using 20% of the entire Waymo *train* set including vanilla *ground truth sam-*

*pling* to fine-tune the detectors. For this, we maintain the same pre-training as in Section 4.1 and utilize these features for SECOND [57], CenterPoint [65] and PV-RCNN [35]. Table 3 shows the results in comparison to these baseline detectors trained from scratch, as well as pre-trained with Voxel-MAE [30].

Although MAELi is tailored for data-efficiency, our self-supervised features are still able to improve the baselines on this large amount of data. Especially for *Pedestrians*, the anchor-based methods benefit from the notion of heading to which our features inherently adapt to. Even though it is hard for a detector to estimate, this is an important clue for path prediction and collision avoidance, in particular, if one considers the vulnerability of this group in traffic.

## 4.3. Ablation Study

We conduct several experiments on the particular aspects of our pipeline. We evaluate the impact of each, the *distance weighting* for free voxels, our *LiDAR-aware reconstruction* objective and compare the two employed masking strategies, *voxel-* and *spherical masking*. Therefore, we pre-train according to the protocol depicted in Section 4.1 and fine-tune a SECOND [57] model on 1% of the latter 399 sequences of the Waymo *train* set. To disable *distance weighting*, we set  $w_j^{D,s} = 1$  for all *free* voxels  $\mathbf{v}_j^{D,s}$ . To disable our *LiDAR-aware reconstruction*, we additionally consider all *unknown* voxels as *free*.

We state the results in Table 4 on *Vehicle* LEVEL 2 across the distance ranges [0m, 30m), [30m, 50m) and [50m,  $+\infty$ ). Our *LiDAR-aware reconstruction* objective

Fraction Labeled Data	Method	3D AP/APH (LEVEL 2)				
		Gain	Overall	Vehicle	Pedestrian	Cyclist
1% (791 frames)	Baseline [57]	- / -	31.09 / 22.25	41.64 / 40.02	33.39 / 17.45	18.24 / 9.29
	MAELi	<b>+14.92 / +10.79</b>	<b>46.01 / 33.05</b>	<b>51.05 / 50.11</b>	<b>48.13 / 24.65</b>	<b>38.86 / 24.38</b>
5% (3952 frames)	Baseline [57]	- / -	46.67 / 34.05	53.19 / 52.37	44.77 / 22.80	42.04 / 26.97
	ProficientTeachers [63]	+4.43 / +11.70	51.10 / 45.75	53.04 / 52.54	50.33 / 38.67	<b>49.92 / 46.03</b>
	MAELi	<b>+6.29 / +13.94</b>	<b>52.96 / 47.99</b>	<b>57.50 / 56.75</b>	<b>53.45 / 41.27</b>	47.93 / 45.94
10% (7904 frames)	Baseline [57]	- / -	52.74 / 38.23	58.11 / 57.46	52.26 / 28.15	47.85 / 29.07
	ProficientTeachers [63]	+2.27 / +12.20	55.01 / 50.43	57.59 / 56.92	54.28 / 43.19	<b>53.15 / 51.18</b>
	MAELi	<b>+3.23 / +13.61</b>	<b>55.97 / 51.84</b>	<b>60.13 / 59.47</b>	<b>55.89 / 45.52</b>	51.90 / 50.52
20% (15808 frames)	Baseline [57]	- / -	55.82 / 51.26	60.16 / 59.54	54.28 / 43.30	53.03 / 50.93
	ProficientTeachers [63]	<b>+2.77 / +2.90</b>	<b>58.59 / 54.16</b>	59.97 / 59.36	57.88 / 46.97	<b>57.93 / 56.15</b>
	MAELi	+2.27 / +2.75	58.09 / 54.01	<b>61.80 / 61.21</b>	<b>57.91 / 47.63</b>	54.57 / 53.18

Table 2. Quantitative results of our features on SECOND [57] on the Waymo *val* set. We use the first 399 sequences of the Waymo *train* set for pre-training and different fractions of the latter 399 sequences for fine-tuning. ProficientTeachers, a semi-supervised method, employs random sampling on the data.

Method	3D AP/APH (LEVEL 2)			
	Overall	Vehicle	Pedestrian	Cyclist
SECOND	58.26 / 54.35	62.58 / 62.02	57.22 / 47.49	54.97 / 53.53
SECOND + Voxel-MAE	59.11 / 55.10	62.67 / 62.34	59.03 / 48.79	55.62 / 54.17
SECOND + MAELi	<b>60.57 / 56.69</b>	<b>63.75 / 63.20</b>	<b>60.71 / 50.93</b>	<b>57.26 / 55.95</b>
Centerpoint	64.51 / 61.92	63.16 / 62.65	64.27 / 58.23	66.11 / 64.87
Centerpoint + Voxel-MAE	<b>65.86 / 63.23</b>	64.05 / 63.53	65.78 / 59.62	<b>67.76 / 66.53</b>
Centerpoint + MAELi	65.60 / 63.00	<b>64.22 / 63.70</b>	<b>65.93 / 59.79</b>	66.66 / 65.52
PV-RCNN	64.84 / 60.86	67.44 / 66.80	63.70 / 53.95	63.39 / 61.82
PV-RCNN + Voxel-MAE	<b>65.82 / 61.98</b>	<b>67.94 / 67.34</b>	64.91 / 55.57	<b>64.62 / 63.02</b>
PV-RCNN + MAELi	65.72 / <b>62.15</b>	67.90 / <b>67.34</b>	<b>65.14 / 56.32</b>	64.13 / 62.79

Table 3. Performance comparison on the Waymo *val* set trained on 20% of the Waymo *train* set. We compare SECOND [57], Centerpoint [65] and PV-RCNN [35] trained from scratch with their pendants utilizing pre-trained weights from Voxel-MAE [30] and MAELi.

improves the overall results across all classes. While *voxel masking* naturally has a nearly equal impact over all ranges, our *spherical masking* is especially beneficial for the range [30m, 50m) with a gain of 1.87AP and 2.01APH (a detailed evaluation on the fraction of masked voxels is provided in the supplemental material). The overall lower impact on the far distance range (above 50m) is also reasonable, since at this distance only very few points hit the same object.

## 5. Conclusion

We proposed MAELi, a self-supervised pre-training approach, carefully designed to adapt to the inherent but subtle properties of large-scale LiDAR point clouds. We were the first to put aspects like occlusion and intrinsic spherical sampling of LiDAR data into the context of SSRL. Our learned representation is especially useful if only few labeled data is available, where it leads to significant improvements. With MAELi, we offer a new method to sustainably

reduce the amount of tedious and costly annotation tasks for LiDAR point clouds.

Method	Overall	3D AP/APH (LEVEL 2)		
		[0m, 30m)	[30m, 50m)	[50m, +inf)
MAELi	51.05 / 50.11	80.22 / 79.37	48.86 / 47.64	21.09 / 19.98
w/o DW	50.91 / 49.85	79.95 / 79.04	48.62 / 47.20	21.47 / 20.31
w/o LAR	50.05 / 48.87	79.33 / 78.20	47.77 / 46.27	20.66 / 19.56
w/o VM	48.99 / 47.86	78.45 / 77.46	46.43 / 45.05	19.47 / 18.23
w/o SM	49.90 / 48.85	79.50 / 78.54	46.99 / 45.63	20.53 / 19.37
Baseline	41.64 / 40.02	72.59 / 70.79	37.09 / 34.86	13.14 / 11.96

Table 4. Impact of the components of MAELi evaluated on the Waymo *val* set for *Vehicle*. We disable *distance weighting* (w/o DW), *LiDAR aware reconstruction* (w/o LAR), *voxel masking* (w/o VM) and *spherical masking* (w/o SM). We use the first 399 sequences of the Waymo *train* set for pre-training and 1% of the second 399 sequences for fine-tuning. We utilize a SECOND [57] model and state a version trained from scratch as baseline.



## References

- [1] Panos Achlioptas, Olga Diamanti, Ioannis Mitliagkas, and Leonidas Guibas. Learning Representations and Generative Models for 3D Point Clouds. In *Proc. ICML*, 2018. 1
- [2] Alex Bewley, Pei Sun, Thomas Mensink, Dragomir Anguelov, and Cristian Sminchisescu. Range Conditioned Dilated Convolutions for Scale Invariant 3D Object Detection. In *Proc. of Conference on Robot Learning*, 2020. 2
- [3] Angel X. Chang, Thomas Funkhouser, Leonidas Guibas, Pat Hanrahan, Qixing Huang, Zimo Li, Silvio Savarese, Manolis Savva, Shuran Song, Hao Su, Jianxiong Xiao, Li Yi, and Fisher Yu. ShapeNet: An Information-Rich 3D Model Repository. *arXiv:1512.03012*, 2015. 1, 3
- [4] Ting Chen, Simon Kornblith, Mohammad Norouzi, and Geoffrey Hinton. A Simple Framework for Contrastive Learning of Visual Representations. In *Proc. ICML*, 2020. 3
- [5] Christopher Choy, JunYoung Gwak, and Silvio Savarese. 4D Spatio-Temporal ConvNets: Minkowski Convolutional Neural Networks. In *Proc. CVPR*, 2019. 3, 4, 6
- [6] Jacob Devlin, Ming-Wei Chang, Kenton Lee, and Kristina Toutanova. BERT: Pre-training of Deep Bidirectional Transformers for Language Understanding. In *Proc. of the Conference of the North American Chapter of the Association for Computational Linguistics: Human Language Technologies*, 2019. 3
- [7] Lue Fan, Xuan Xiong, Feng Wang, Naiyan Wang, and Zhaoxiang Zhang. RangeDet: In Defense of Range View for LiDAR-based 3D Object Detection. *arXiv:2103.10039*, 2021. 2
- [8] Andreas Geiger, Philip Lenz, and Raquel Urtasun. Are we ready for autonomous driving? The KITTI vision benchmark suite. In *Proc. CVPR*, 2012. 6
- [9] Rohit Girdhar, David F. Fouhey, Mikel Rodriguez, and Abhinav Gupta. Learning a Predictable and Generative Vector Representation for Objects. In *Proc. ECCV*, 2016. 3
- [10] Benjamin Graham, Martin Engelcke, and Laurens van der Maaten. 3D Semantic Segmentation With Submanifold Sparse Convolutional Networks. In *Proc. CVPR*, 2018. 4
- [11] Tianrui Guan, Jun Wang, Shiyi Lan, Rohan Chandra, Zuxuan Wu, Larry Davis, and Dinesh Manocha. M3DETR: Multi-Representation, Multi-Scale, Mutual-Relation 3D Object Detection With Transformers. In *Proc. WACV*, 2022. 2
- [12] Chenhang He, Hui Zeng, Jianqiang Huang, Xian-Sheng Hua, and Lei Zhang. Structure Aware Single-Stage 3D Object Detection From Point Cloud. In *Proc. CVPR*, 2020. 2
- [13] Kaiming He, Xinlei Chen, Saining Xie, Yanghao Li, Piotr Dollár, and Ross Girshick. Masked Autoencoders Are Scalable Vision Learners. In *Proc. CVPR*, 2022. 3
- [14] Kaiming He, Haoqi Fan, Yuxin Wu, Saining Xie, and Ross Girshick. Momentum Contrast for Unsupervised Visual Representation Learning. In *Proc. CVPR*, 2020. 3
- [15] Georg Hess, Johan Jaxing, Elias Svensson, David Hagerman, Christoffer Petersson, and Lennart Svensson. Masked Autoencoders for Self-Supervised Learning on Automotive Point Clouds. *arXiv:2207.00531*, 2022. 1, 3
- [16] R. Devon Hjelm, Alex Fedorov, Samuel Lavoie-Marchildon, Karan Grewal, Phil Bachman, Adam Trischler, and Yoshua Bengio. Learning deep representations by mutual information estimation and maximization. In *Proc. ICLR*, 2019. 3
- [17] Jordan S. K. Hu, Tianshu Kuai, and Steven L. Waslander. Point Density-Aware Voxels for LiDAR 3D Object Detection. In *Proc. CVPR*, 2022. 2
- [18] Peiyun Hu, Jason Ziglar, David Held, and Deva Ramanan. What You See is What You Get: Exploiting Visibility for 3D Object Detection. In *Proc. CVPR*, 2020. 3
- [19] Siyuan Huang, Yichen Xie, Song-Chun Zhu, and Yixin Zhu. Spatio-Temporal Self-Supervised Representation Learning for 3D Point Clouds. In *Proc. ICCV*, 2021. 3
- [20] Diederik P. Kingma and Jimmy Ba. Adam: A Method for Stochastic Optimization. *arXiv:1412.6980*, 2017. 6
- [21] Alex H. Lang, Sourabh Vora, Holger Caesar, Lubing Zhou, Jiong Yang, and Oscar Beijbom. PointPillars: Fast Encoders for Object Detection From Point Clouds. In *Proc. CVPR*, 2019. 2
- [22] Bo Li, Tianlei Zhang, and Tian Xia. Vehicle Detection from 3D Lidar Using Fully Convolutional Network. In *Robotics: Science and Systems*, 2016. 2
- [23] Zhichao Li, Feng Wang, and Naiyan Wang. LiDAR R-CNN: An Efficient and Universal 3D Object Detector. In *Proc. CVPR*, 2021. 2
- [24] Hanxue Liang, Chenhan Jiang, Dapeng Feng, Xin Chen, Hang Xu, Xiaodan Liang, Wei Zhang, Zhenguo Li, and Luc Van Gool. Exploring Geometry-Aware Contrast and Clustering Harmonization for Self-Supervised 3D Object Detection. In *Proc. ICCV*, 2021. 3
- [25] Haotian Liu, Mu Cai, and Yong Jae Lee. Masked Discrimination for Self-Supervised Learning on Point Clouds. In *Proc. ECCV*, 2022. 1, 3
- [26] Jiageng Mao, Minzhe Niu, Haoyue Bai, Xiaodan Liang, Hang Xu, and Chunjing Xu. Pyramid R-CNN: Towards Better Performance and Adaptability for 3D Object Detection. In *Proc. ICCV*, 2021. 2
- [27] Jiageng Mao, Yujing Xue, Minzhe Niu, Haoyue Bai, Jiashi Feng, Xiaodan Liang, Hang Xu, and Chunjing Xu. Voxel Transformer for 3D Object Detection. In *Proc. ICCV*, 2021. 2
- [28] Gregory P. Meyer, Ankit Laddha, Eric Kee, Carlos Vallespi-Gonzalez, and Carl K. Wellington. LaserNet: An Efficient Probabilistic 3D Object Detector for Autonomous Driving. In *Proc. CVPR*, 2019. 2
- [29] Zhenwei Miao, Jikai Chen, Hongyu Pan, Ruiwen Zhang, Kaixuan Liu, Peihan Hao, Jun Zhu, Yang Wang, and Xin Zhan. PVGNet: A Bottom-Up One-Stage 3D Object Detector With Integrated Multi-Level Features. In *Proc. CVPR*, 2021. 2
- [30] Chen Min, Xinli Xu, Dawei Zhao, Liang Xiao, Yiming Nie, and Bin Dai. Voxel-MAE: Masked Autoencoders for Pre-training Large-scale Point Clouds. *arXiv:2206.09900*, 2022. 1, 3, 7, 8
- [31] Yatian Pang, Wenxiao Wang, Francis E. H. Tay, Wei Liu, Yonghong Tian, and Li Yuan. Masked Autoencoders for Point Cloud Self-supervised Learning. In *Proc. ECCV*, 2022. 1, 3, 6

- [32] Charles R. Qi, Hao Su, Kaichun Mo, and Leonidas J. Guibas. PointNet: Deep Learning on Point Sets for 3D Classification and Segmentation. In *Proc. CVPR*, 2017. 2
- [33] Charles Ruizhongtai Qi, Li Yi, Hao Su, and Leonidas J Guibas. PointNet++: Deep Hierarchical Feature Learning on Point Sets in a Metric Space. In *Adv. NeurIPS*, 2017. 2
- [34] Hualian Sheng, Sijia Cai, Yuan Liu, Bing Deng, Jianqiang Huang, Xian-Sheng Hua, and Min-Jian Zhao. Improving 3D Object Detection With Channel-Wise Transformer. In *Proc. ICCV*, 2021. 2
- [35] Shaoshuai Shi, Chaoxu Guo, Li Jiang, Zhe Wang, Jianping Shi, Xiaogang Wang, and Hongsheng Li. PV-RCNN: Point-Voxel Feature Set Abstraction for 3D Object Detection. In *Proc. CVPR*, 2020. 2, 6, 7, 8
- [36] Shaoshuai Shi, Li Jiang, Jiajun Deng, Zhe Wang, Chaoxu Guo, Jianping Shi, Xiaogang Wang, and Hongsheng Li. PV-RCNN++: Point-Voxel Feature Set Abstraction With Local Vector Representation for 3D Object Detection. *arXiv:2102.00463*, 2022. 2
- [37] Shaoshuai Shi, Xiaogang Wang, and Hongsheng Li. PointRCNN: 3D Object Proposal Generation and Detection From Point Cloud. In *Proc. CVPR*, 2019. 2
- [38] Shaoshuai Shi, Zhe Wang, Jianping Shi, Xiaogang Wang, and Hongsheng Li. From Points to Parts: 3D Object Detection From Point Cloud With Part-Aware and Part-Aggregation Network. *PAMI*, 43(08):2647–2664, 2021. 2, 4
- [39] Weijing Shi and Raj Rajkumar. Point-GNN: Graph Neural Network for 3D Object Detection in a Point Cloud. In *Proc. CVPR*, 2020. 2
- [40] Leslie N. Smith. A disciplined approach to neural network hyper-parameters: Part 1 – learning rate, batch size, momentum, and weight decay. *arXiv:1803.09820*, 2018. 6
- [41] Pei Sun, Henrik Kretschmar, Xerxes Dotiwalla, Aurelien Chouard, Vijaysai Patnaik, Paul Tsui, James Guo, Yin Zhou, Yuning Chai, Benjamin Caine, Vijay Vasudevan, Wei Han, Jiquan Ngiam, Hang Zhao, Aleksei Timofeev, Scott Ettinger, Maxim Krivokon, Amy Gao, Aditya Joshi, Yu Zhang, Jonathon Shlens, Zhifeng Chen, and Dragomir Anguelov. Scalability in Perception for Autonomous Driving: Waymo Open Dataset. In *Proc. CVPR*, 2020. 1, 2, 6, 12
- [42] Pei Sun, Mingxing Tan, Weiyue Wang, Chenxi Liu, Fei Xia, Zhaoqi Leng, and Dragomir Anguelov. SWFormer: Sparse Window Transformer for 3D Object Detection in Point Clouds. In *Proc. ECCV*, 2022. 2
- [43] OpenPCDet Development Team. OpenPCDet: An Open-source Toolbox for 3D Object Detection from Point Clouds. <https://github.com/open-mmlab/OpenPCDet>, 2020. 6
- [44] Darren Tsai, Julie Stephany Berrio, Mao Shan, Eduardo Nebot, and Stewart Worrall. Viewer-Centred Surface Completion for Unsupervised Domain Adaptation in 3D Object Detection. *arXiv:2209.06407*, 2022. 3
- [45] Ashish Vaswani, Noam Shazeer, Niki Parmar, Jakob Uszkoreit, Llion Jones, Aidan N Gomez, Łukasz Kaiser, and Illia Polosukhin. Attention is All you Need. In *Adv. NeurIPS*, 2017. 2
- [46] Hanchen Wang, Qi Liu, Xiangyu Yue, Joan Lasenby, and Matt J. Kusner. Unsupervised Point Cloud Pre-Training via Occlusion Completion. In *Proc. ICCV*, 2021. 1, 3
- [47] Wenguan Wang, Tianfei Zhou, Fisher Yu, Jifeng Dai, Ender Konukoglu, and Luc Van Gool. Exploring Cross-Image Pixel Contrast for Semantic Segmentation. In *Proc. ICCV*, 2021. 3
- [48] Yan Wang, Xiangyu Chen, Yurong You, Li Erran Li, Bharath Hariharan, Mark Campbell, Kilian Q. Weinberger, and Wei-Lun Chao. Train in Germany, Test in the USA: Making 3D Object Detectors Generalize. In *Proc. CVPR*, 2020. 1
- [49] Yue Wang, Alireza Fathi, Abhijit Kundu, David A. Ross, Caroline Pantofaru, Tom Funkhouser, and Justin Solomon. Pillar-Based Object Detection for Autonomous Driving. In *Proc. ECCV*, 2020. 2
- [50] Xin Wen, Tianyang Li, Zhizhong Han, and Yu-Shen Liu. Point Cloud Completion by Skip-Attention Network With Hierarchical Folding. In *Proc. CVPR*, 2020. 1
- [51] Zhirong Wu, Shuran Song, Aditya Khosla, Fisher Yu, Linguang Zhang, Xiaoou Tang, and Jianxiong Xiao. 3D ShapeNets: A Deep Representation for Volumetric Shapes. In *Proc. CVPR*, 2015. 1, 3
- [52] Guangda Xie, Yang Li, Hongquan Qu, and Zaiming Sun. Masked Autoencoder for Pre-Training on 3D Point Cloud Object Detection. *Mathematics*, 10(19):3549, 2022. 3
- [53] Saining Xie, Jiatao Gu, Demi Guo, Charles R. Qi, Leonidas Guibas, and Or Litany. PointContrast: Unsupervised Pre-training for 3D Point Cloud Understanding. In *Proc. ECCV*, 2020. 3
- [54] Qiangeng Xu, Yiqi Zhong, and Ulrich Neumann. Behind the Curtain: Learning Occluded Shapes for 3D Object Detection. In *Proc. AAAI*, 2022. 3
- [55] Qiangeng Xu, Yin Zhou, Weiyue Wang, Charles R. Qi, and Dragomir Anguelov. SPG: Unsupervised Domain Adaptation for 3D Object Detection via Semantic Point Generation. In *Proc. ICCV*, 2021. 3
- [56] Siming Yan, Zhenpei Yang, Haoxiang Li, Li Guan, Hao Kang, Gang Hua, and Qixing Huang. Implicit Autoencoder for Point Cloud Self-supervised Representation Learning. *arXiv:2201.00785*, 2022. 3
- [57] Yan Yan, Yuxing Mao, and Bo Li. SECOND: Sparsely Embedded Convolutional Detection. *Sensors*, 18(10):3337, 2018. 2, 3, 4, 6, 7, 8, 12, 14
- [58] Bin Yang, Wenjie Luo, and Raquel Urtasun. PIXOR: Real-Time 3D Object Detection From Point Clouds. In *Proc. CVPR*, 2018. 2
- [59] Juyoung Yang, Pyunghwan Ahn, Doyeon Kim, Haeil Lee, and Junmo Kim. Progressive Seed Generation Auto-Encoder for Unsupervised Point Cloud Learning. In *Proc. ICCV*, 2021. 3
- [60] Zetong Yang, Yanan Sun, Shu Liu, and Jiaya Jia. 3DSSD: Point-Based 3D Single Stage Object Detector. In *Proc. CVPR*, 2020. 2
- [61] Zetong Yang, Yanan Sun, Shu Liu, Xiaoyong Shen, and Jiaya Jia. STD: Sparse-to-Dense 3D Object Detector for Point Cloud. In *Proc. ICCV*, 2019. 2

- [62] Maosheng Ye, Shuangjie Xu, and Tongyi Cao. HVNet: Hybrid Voxel Network for LiDAR Based 3D Object Detection. In *Proc. CVPR*, 2020. 2
- [63] Junbo Yin, Jin Fang, Dingfu Zhou, Liangjun Zhang, Cheng-Zhong Xu, Jianbing Shen, and Wenguan Wang. Semi-supervised 3D Object Detection with Proficient Teachers. In *Proc. ECCV*, 2022. 7, 8
- [64] Junbo Yin, Dingfu Zhou, Liangjun Zhang, Jin Fang, Cheng-Zhong Xu, Jianbing Shen, and Wenguan Wang. Proposal-Contrast: Unsupervised Pre-training for LiDAR-based 3D Object Detection. In *Proc. ECCV*, 2022. 3
- [65] Tianwei Yin, Xingyi Zhou, and Philipp Krähenbühl. Center-Based 3D Object Detection and Tracking. In *Proc. CVPR*, 2021. 2, 6, 7, 8
- [66] Xumin Yu, Lulu Tang, Yongming Rao, Tiejun Huang, Jie Zhou, and Jiwen Lu. Point-BERT: Pre-Training 3D Point Cloud Transformers With Masked Point Modeling. In *Proc. CVPR*, 2022. 1, 3, 6
- [67] Yifan Zhang, Qingyong Hu, Guoquan Xu, Yanxin Ma, Jianwei Wan, and Yulan Guo. Not All Points Are Equal: Learning Highly Efficient Point-Based Detectors for 3D LiDAR Point Clouds. In *Proc. CVPR*, 2022. 2
- [68] Zaiwei Zhang, Rohit Girdhar, Armand Joulin, and Ishan Misra. Self-Supervised Pretraining of 3D Features on Any Point-Cloud. In *Proc. ICCV*, 2021. 3
- [69] Xingyi Zhou, Dequan Wang, and Philipp Krähenbühl. Objects as Points. *arXiv:1904.07850*, 2019. 2
- [70] Yin Zhou and Oncel Tuzel. VoxelNet: End-to-End Learning for Point Cloud Based 3D Object Detection. In *Proc. CVPR*, 2018. 2

## A. Supplemental Material

This supplemental material presents further details, results and insights. We describe the detailed architecture of our decoder in Appendix A.1, evaluate the impact of different amounts of masked voxels in Appendix A.2 and discuss potential limitations in Appendix A.3. Finally, we discuss some additional insights on reconstruction results and data-efficiency in Appendix A.4.

### A.1. Sparse Reconstruction Decoder

To describe the architecture of our decoder in detail, we group operations with the same *voxel/tensor stride* into a *block*. In Table 5, we list the different decoder blocks in addition to the preceding SECOND encoder (summarized as single entry) and the required *reshaping+sampling* step to transform the dense feature representation back to a sparse 3D tensor.

Description	# Channels	Voxel/Tensor Stride	Spatial Dimension
SECOND Encoder	512	-	188 × 188
Reshaping + Sampling	256	8 × 8 × 16	188 × 188 × 2
DBlock 1	64	8 × 8 × 8	188 × 188 × 5
DBlock 2	64	4 × 4 × 4	376 × 376 × 11
DBlock 3	32	2 × 2 × 2	752 × 752 × 21
DBlock 4	16	1 × 1 × 1	1504 × 1504 × 41

Table 5. Architecture of our decoder. We state the number of channels, the voxel stride and the maximum spatial dimension for the Waymo Open Dataset [41] after each block. Stride and spatial dimensions are depicted in the format  $x \times y \times z$ . Each decoder block *inverts* one downsampling step from the encoder, eventually resulting in the original voxel stride.

Each block consists, among others, of an upsampling- and pruning step. For upsampling, we utilize a *generative transposed convolution* and for pruning, we use a  $1 \times 1 \times 1$  submanifold sparse convolution to create the required classification score. The respective operations of each block are listed in Table 6.

### A.2. Ablation Study Voxel Masking

We evaluated our *voxel masking* under different amounts of voxels. We maintain the training and evaluation scheme from the ablation study in the main paper and vary the amount of kept voxels. The results are shown in Table 7. Overall, keeping 60% of the voxels lead to the best overall results, eventually used for all other experiments with MAELi. However, in combination with *spherical masking* significantly fewer points than this fraction actually remain. To get an estimate, we evaluated the amount of effectively used points over 10000 iterations, resulting in a fraction of 15.57% on average.

Operation	Kernel Size	Stride
Generative Transposed Convolution	$2 \times 2 \times 2^\dagger$	$2 \times 2 \times 2^\dagger$
Batch Norm	-	-
ReLU	-	-
Submanifold Sparse Convolution	$3 \times 3 \times 3$	$1 \times 1 \times 1$
Batch Norm	-	-
ReLU	-	-
Submanifold Sparse Convolution	$1 \times 1 \times 1$	$1 \times 1 \times 1$
Pruning	-	-

Table 6. Structure of each decoder block. We additionally state the operation’s kernel size and stride, each in the format  $x \times y \times z$ . The upper part depicts the upsampling and feature transformation. The lower part uses the final feature representation from above and decides via classification whether a voxels is pruned or not. <sup>†</sup>These values deviate for DBlock 1, where it has a kernel size of  $1 \times 1 \times 3$  and a stride of  $1 \times 1 \times 2$  to invert the encoder’s respective downsampling step.

Fraction Voxels	3D AP/APH (LEVEL 2)			
	Overall	Vehicle	Pedestrian	Cyclist
0.8	45.34 / 32.84	50.26 / 49.10	48.03 / 24.33	37.74 / <b>25.09</b>
0.7	44.91 / 32.10	50.35 / 49.19	47.54 / 24.29	36.83 / 22.83
0.6	<b>46.01 / 33.05</b>	<b>51.05 / 50.11</b>	48.13 / <b>24.65</b>	<b>38.86 / 24.38</b>
0.5	45.60 / 32.27	50.87 / 49.79	47.08 / 23.72	<b>38.86 / 23.31</b>
0.4	45.79 / 31.85	50.36 / 49.24	<b>48.27 / 24.50</b>	38.74 / 21.81
Baseline	31.09 / 22.25	41.64 / 40.02	33.39 / 17.45	18.24 / 9.29

Table 7. Impact of different amounts of voxels kept during *voxel masking* evaluated on the Waymo *val* set for *Vehicle*. We use the first 399 sequences of the Waymo *train* set for pre-training and 1% of the second 399 sequences for fine-tuning. We utilize a SECOND [57] model and state a version trained from scratch as baseline.

### A.3. Limitations

Even though our sparse decoder allows for a memory efficient reconstruction, the amount of reconstructed voxels is obviously not unlimited. Especially during the first iterations of our pre-training, while not sufficiently trained, some samples lead to an uncontrolled reconstruction. In order to regulate the amount of reconstructed voxels and to avoid training breakdowns, we introduce two limiting factors. First, we prune all reconstructed voxels 0.1m below the ego vehicle, since these are below the ground plane and thus, typically provide no useful contribution. Second, we introduce a threshold for maximum amount of reconstructed voxels to ensure that we do not run into memory issues. If an upsampling step would generate more voxels than this limit, we randomly prune before the upsampling. For these pruned voxels, simply no loss is induced, which only slightly *delays* the training effect for these rare cases. We set the maximum number of total voxels to 6 million, which are easily processable on an NVIDIA® GeForce® RTX 3090 GPU and counted only 62 limit exceedances within the first 10k iterations of a random experiment.

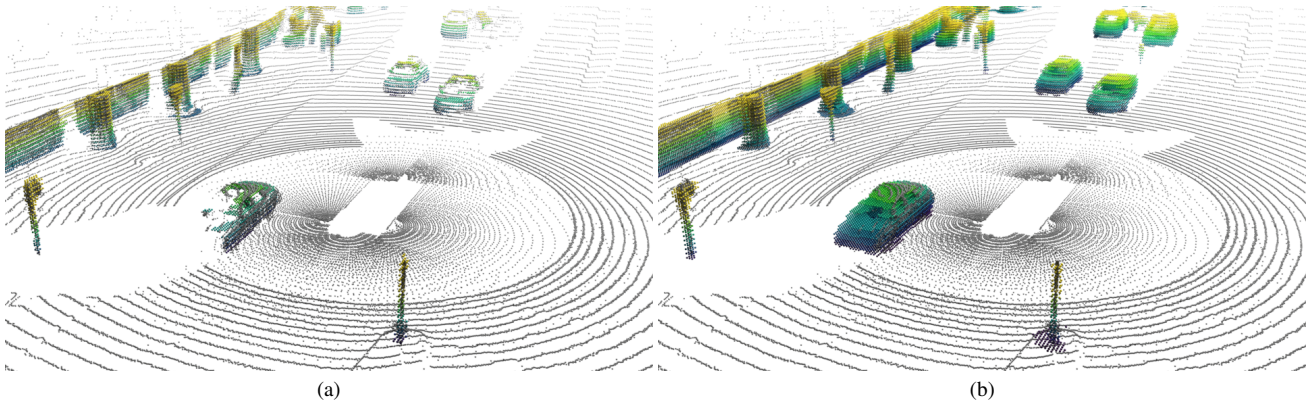


Figure 5. Completion results without (a) and with (b) our *LiDAR aware reconstruction* on a full point cloud (gray). For visualization purposes, we color-coded the output points by their  $z$ -coordinate and removed the reconstructed ground plane.

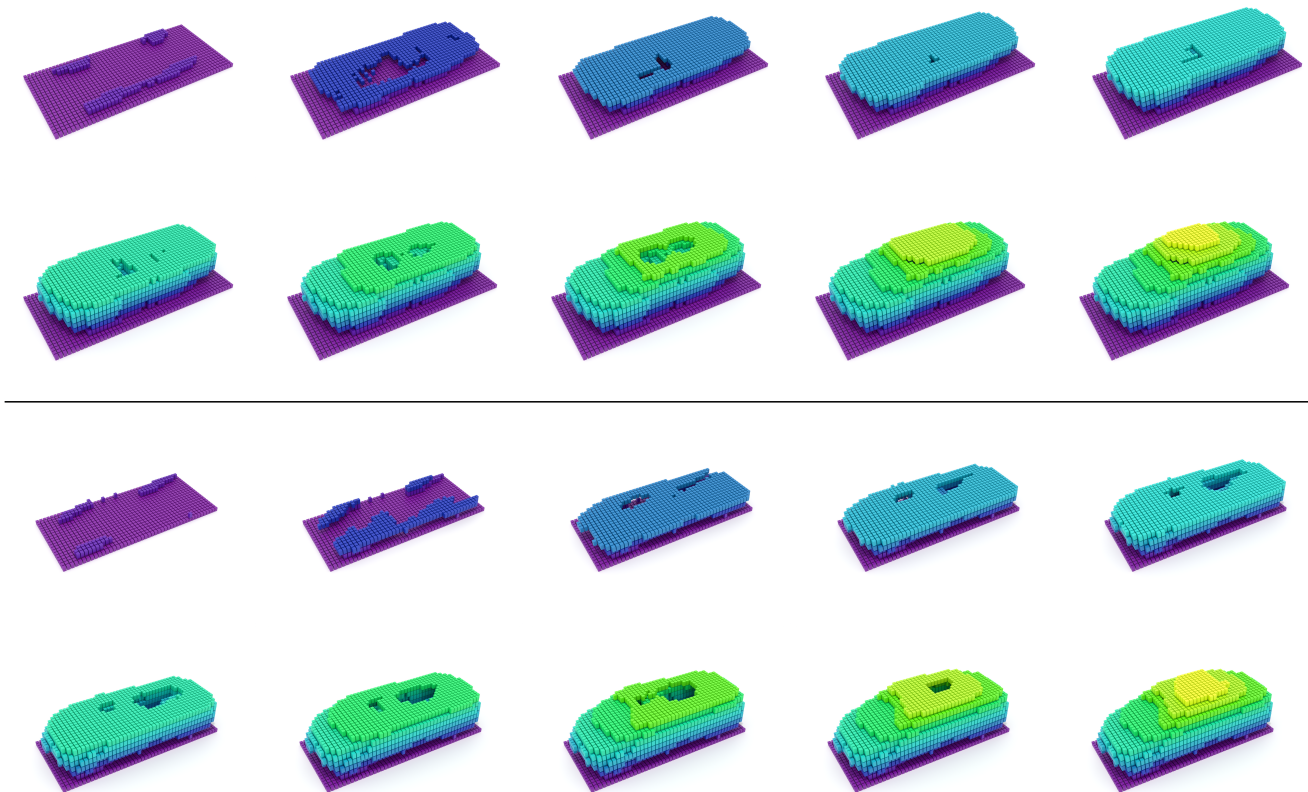


Figure 6. Different layers of two reconstructed cars. We often observed, that the reconstructed cars are often hollow. There are visible tendencies to leave parts of the interior free and reconstruct the sampled surface only.

#### A.4. Additional Insights

**Reconstruction Capabilities:** In Figure 5, we visualize the completion capabilities of our *LiDAR aware loss* on a full point cloud. It encourages the network to fill up gaps in the

wall and reconstruct the occluded areas of cars.

In Figure 6, we show the individual layers of two different reconstructed cars. We can see that our pretraining scheme indeed encourages the model to go beyond the sampled LiDAR surface, reconstructing the entire car, also

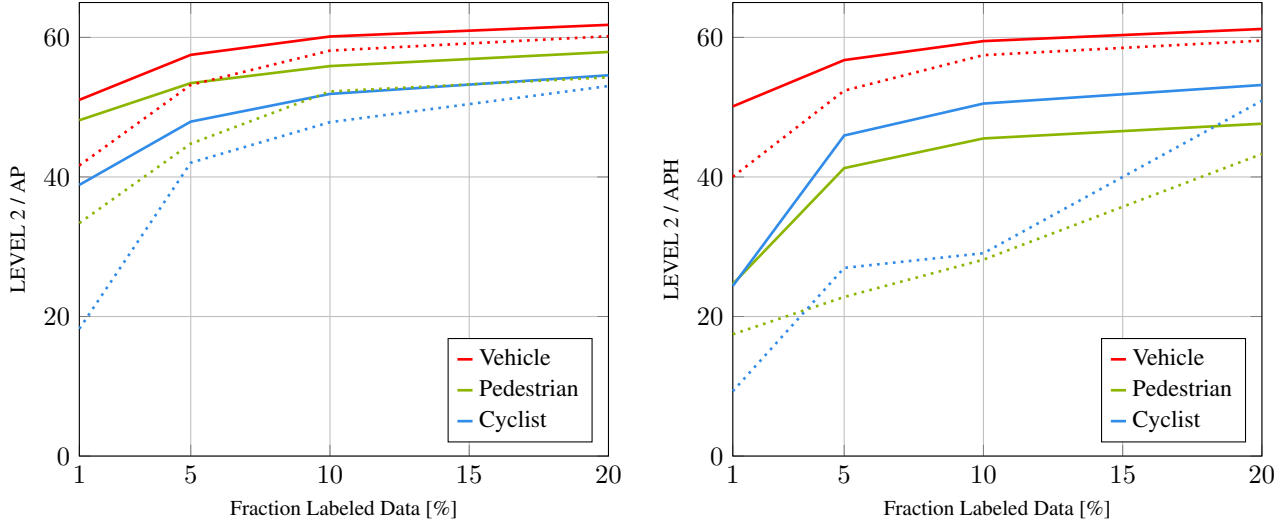


Figure 7. Results of our features on SECOND [57] on the Waymo *val* set, using different amounts of labeled data. We use the first 399 sequences of the Waymo *train* set without any labels for pre-training and different fractions of the latter 399 sequences for fine-tuning. The *solid lines* are the results utilizing our features pre-trained with MAELi. The *dotted lines* denote the version trained from scratch.

showing some hints for the correct placement of tires. Furthermore, especially parts of the interior, which are often surrounded by glass and thus, sometimes traversed by LiDAR beams, are seemingly left out during the reconstruction.

**AP vs APH Data Efficiency:** In Figure 7, we plot the data efficiency results using our MAELi-based pre-training on the SECOND [57] detector. All three classes benefit from our pre-training (solid lines) compared to the version trained from scratch (dotted lines). With little data, the detector especially struggles to estimate the heading, which can be clearly seen for the smaller, less represented classes *Pedestrian* and *Cyclist*. However, utilizing our features, a proper estimation and significant detection improvements are possible already, early on, with only few annotated data samples.